

# Direct Visualization of Phase-Locking of Large Josephson Junction Arrays by Surface Electromagnetic Waves


M.A. Galin<sup>1,2</sup>, F. Rudau,<sup>3</sup> E.A. Borodianskiy,<sup>4</sup> V.V. Kurin,<sup>1</sup> D. Koelle,<sup>3</sup> R. Kleiner,<sup>3</sup>  
V.M. Krasnov<sup>1,2,\*</sup> and A.M. Klushin<sup>1</sup>

<sup>1</sup>*Institute for Physics of Microstructures RAS, Nizhny Novgorod 603950, Russia*

<sup>2</sup>*Moscow Institute of Physics and Technology, Dolgoprudny 141700, Moscow Province, Russia*

<sup>3</sup>*Physikalisches Institut, Center for Quantum Science and LISA+, Universität Tübingen,  
72076 Tübingen, Germany*

<sup>4</sup>*Department of Physics, Stockholm University, AlbaNova University Center, SE-106 91 Stockholm, Sweden*

 (Received 3 April 2020; revised 13 July 2020; accepted 14 July 2020; published 18 August 2020)

Phase-locking of oscillators leads to super-radiant amplification of the emission power. This is particularly important for development of terahertz sources, which suffer from low emission efficiency. In this work we study large Josephson junction arrays containing several thousand Nb-based junctions. Using low-temperature scanning laser microscopy, we observe that at certain bias conditions two-dimensional standing-wave patterns are formed, manifesting themselves as global synchronization of the arrays. Analysis of standing waves indicates that they are formed by surface plasmon-type electromagnetic waves propagating at the electrode-substrate interface. Thus, we demonstrate that surface waves provide an effective mechanism for long-range coupling and phase-locking of large junction arrays.

DOI: [10.1103/PhysRevApplied.14.024051](https://doi.org/10.1103/PhysRevApplied.14.024051)

## I. INTRODUCTION

The creation of tunable, monochromatic, high-power, and compact sources of electromagnetic (EM) waves in the 0.1–10-THz frequency range remains a serious technological challenge, colloquially known as the “terahertz gap” [1]. Josephson junctions (JJs) have a unique ability to generate EM radiation with tunable frequency  $f = 2eV/h$ , where  $h$  is the Planck constant,  $2e$  is the charge of Cooper pairs, and  $V$  is the dc voltage across the JJs [2–10]. The record tunability range, 1–11 THz [11], has been reported for intrinsic JJs in cuprate high-temperature superconductors, for which the energy gap, determining the upper frequency limit, can be in excess of 20 THz [12,13]. The emission power from a single JJ is low [10]. It can be amplified in the super-radiant manner by phase-locking of many JJs. JJs can be arranged in arrays on two-dimensional planes [14–18], stacked vertically [2,3], or in both ways when stacked JJs are arranged in an array [4,9]. In all cases it is necessary to synchronize the JJs and segments or stacks in the arrays together. However, with increasing number of JJs, their synchronization becomes progressively more difficult due to the rapidly growing number of degrees of freedom.

Synchronization of large JJ arrays requires long-range interaction between JJs. Usually this is mediated by

resonant cavity modes leading to the formation of standing waves either inside [19,20], or outside [15,16] the JJs. With increasing array size, cavity modes become damped by dissipation. For very large arrays, with sizes much larger than the wavelength of emitted radiation, an alternative, nonresonant mechanism of synchronization by traveling waves has been suggested, and synchronization of up to 9000 JJs was demonstrated recently [17,18]. Traveling waves in JJ arrays are essentially surface EM waves (SEMWs) propagating at electrode-substrate or vacuum interfaces. There are a great variety of SEMWs at metal-insulator interfaces (for a review see, e.g., Ref. [21]), including surface plasmons in the infrared range, which are being actively studied from the perspective of the development of plasmonic components for optoelectronic devices [22–29]. SEMWs also exist in superconducting wires [30] and thin films [31]. Most interesting in the context of this work are leaky SEMWs [23], which facilitate emission of EM power into open space.

In this work we study Nb/NbSi/Nb JJ arrays with different geometries, containing 1500 and 1660 JJs. We perform transport measurements, study the emitted EM power using an external bolometer, and use low-temperature scanning laser microscopy (LTSLM) for visualization of wave dynamics in the arrays. The current-voltage characteristics (IVCs) of the arrays exhibit profound current steps, indicating the appearance of cavity-mode resonances in the arrays. The steps are accompanied by enhanced

\*vladimir.krasnov@fysik.su.se

emission of EM waves at Josephson frequencies in the subterahertz range. Using LTSLM imaging, we directly observe the appearance of two-dimensional standing-wave patterns in the arrays at certain bias conditions. Analysis of phase velocities unambiguously indicates that the standing waves are formed by leaky plasmon-type surface EM waves propagating along the electrode-substrate interface. The leakage of SEMW energy into open space facilitates both emission of EM waves and a long-range interaction between junctions in the array, which is needed for mutual phase-locking and super-radiant emission. Thus, we demonstrate that SEMWs traveling along the array provide an effective mechanism for synchronization of very large arrays with sizes much larger than the emitted wavelength.

## II. EXPERIMENT

We study Nb/NbSi/Nb junction arrays made at the Physikalisch-Technische Bundesanstalt, Braunschweig, Germany [32]. We use LTSLM combined with simultaneous transport measurements for the analysis of the electric field distribution in two arrays with different geometries. We also perform detection of electromagnetic wave emission for similar arrays from the same batch under experimental conditions similar to the LTSLM setup. The emission is detected by a high-purity-*n*-doped-InSb bolometer. The characteristics of the bolometer are described in Ref. [18]. The bolometer is oriented face-to-face with the array chip at a distance of 5 mm and detects emission predominantly in the direction perpendicular (normal) to the array surface. Measurements of electromagnetic wave emission outside the cryostat (far field) were performed on similar arrays and showed qualitatively similar results [33]. Transport measurements are performed either in  $^4\text{He}$  (sample in a gas) or in  $^3\text{He}$  (sample in a vacuum) cryostats. All measurements are performed in zero (ambient) magnetic field.

### A. Samples

We study arrays of serially connected Nb/Nb $_x$ Si $_{1-x}$ /Nb ( $x \sim 0.1$ ) JJs, made on oxidized silicon substrates. Figure 1 shows the layouts of the two arrays we study, which we refer to as “linear” [Fig. 1(a)] and “meandering” [Fig. 1(b)]. JJs with size  $8 \times 8 \mu\text{m}^2$  and a repetition period of  $15 \mu\text{m}$  are formed at the overlap between the top and bottom Nb electrodes, as sketched in the inset. The linear array, Fig. 1(a), consists of five long parallel lines, containing 332 JJs each, thus yielding in total  $N_l = 1660$  JJs. The meandering array, Fig. 1(b), consists of 125 transverse strips with length  $290 \mu\text{m}$ . The distance between strips is  $40 \mu\text{m}$ . Each strip contains 12 JJs, yielding  $N_m = 1500$  in total. The overall size of both arrays is 5 mm (from left to right in Fig. 1). More details about the fabrication and characterization can be found in Refs. [32,34]. Transport

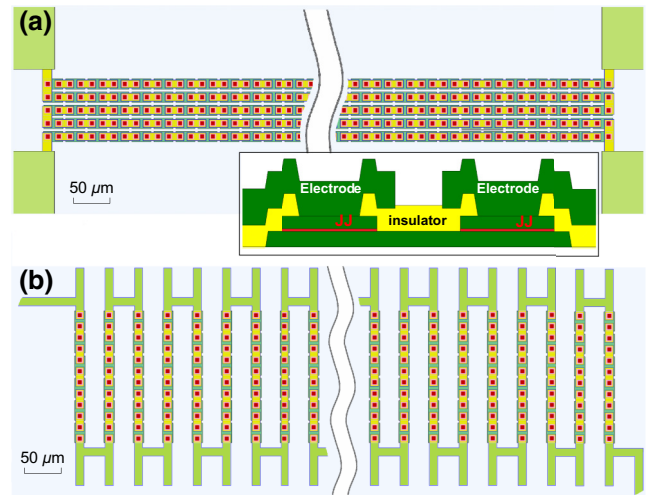


FIG. 1. Geometry of the JJ arrays studied. (a) Top view of the linear array. Red dots represent junctions, yellow and green stripes are Nb electrodes sequentially connecting the JJs, and green rectangles at the corners are contact pads. The inset shows a cross section (side view) of the junction area (from Ref. [32]). (b) Top view of the meanderer array. Contact pads are outside the image area. The vertical wavy lines in (a),(b) indicate a break in the pictures.

properties and emission characteristics of similar arrays can be found in Refs. [17,18,33].

### B. Low-temperature scanning laser microscopy

The LTSLM technique and a similar low-temperature scanning electron microscopy can be used for visualization of standing EM waves in JJs [35–38] and JJ arrays [39–42], as well as for analysis of spatial inhomogeneities in superconducting structures [43,44]. In the LTSLM setup, a sample is mounted inside an optical helium-flow cryostat, where it is typically cooled to 5–6 K by a helium-vapor jet. The beam of a diode laser is directed by a scanning unit to the surface of the sample and is focused to a spot size of  $1\text{--}2 \mu\text{m}$  in diameter. This causes local heating  $\Delta T \lesssim 1$  K, which is small enough not to destroy superconductivity, but large enough to induce measurable changes in IVCs. The LTSLM image is acquired by our applying a certain bias current through the array and measuring the beam-induced voltage response  $\Delta U(x, y)$  on scanning of the laser beam in the  $x$ - $y$  plane. To increase the signal-to-noise ratio, the beam is modulated at 10–80 kHz and  $\Delta U$  is detected by a lock-in amplifier.

In Fig. 2(a) we show the IVC of the linear array measured during the LTSLM imaging. The LTSLM images at bias points  $A$ – $D$ , marked in the IVC, are shown in Fig. 2(b). The horizontal scale of the images is  $L = 0.91$  mm, which is approximately one sixth of the array’s length. The vertical scale is stretched by a factor of 2 for

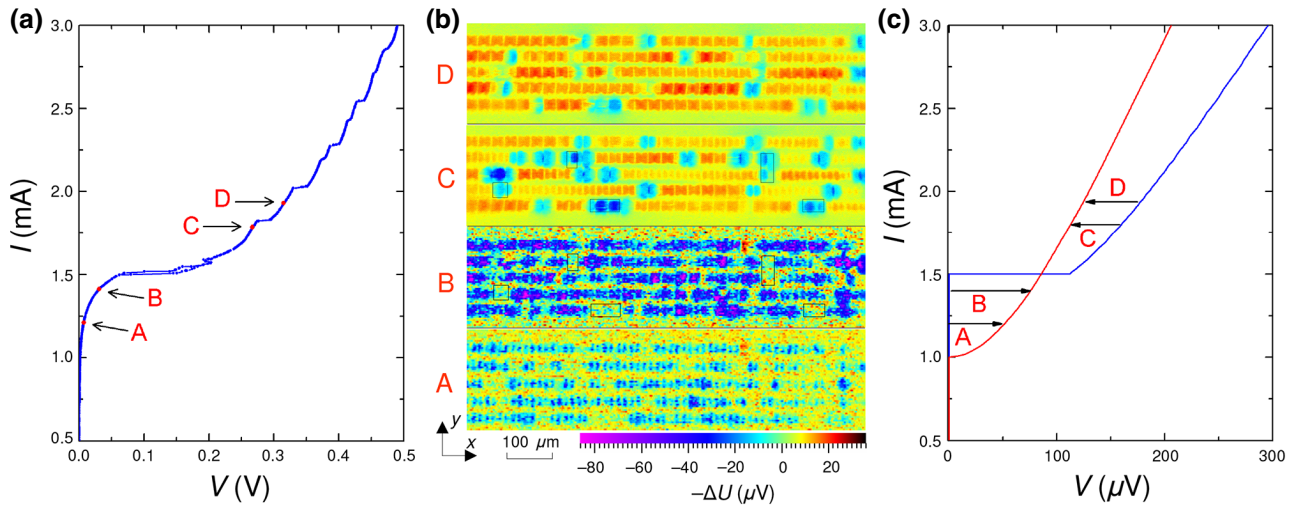


FIG. 2. (a)  $I$ - $V$  characteristic of the linear array measured during LTSLM imaging. (b) LTSLM images obtained at four bias points, indicated in (a). The sign of  $\Delta U$  for most of the JJs changes from positive for bias points  $A$  and  $B$  to negative for bias points  $C$  and  $D$ . (c) Simulation of the LTSLM response from a single JJ. The blue and red lines represent IVCs with the laser beam *off* and *on*, respectively. Heating by the laser beam leads to suppression of the critical current and reduction of the junction resistance due to the semiconducting nature of the NbSi barrier. This leads to the sign change of the LTSLM response from positive for points  $A$  and  $B$  to negative for points  $C$  and  $D$ .

better visibility. In all images five horizontal array lines can be seen with square-shaped (due to vertical stretching) top Nb electrodes covering two JJs; see Fig. 1(a). Bias point  $A$ ,  $I = 1.2$  mA, and bias point  $B$ ,  $I = 1.4$  mA, are below the critical current  $I_c \simeq 1.5$  mA. In this case the LTSLM response is mostly positive,  $\Delta U > 0$ . However, for bias point  $C$ ,  $I = 1.78$  mA, and bias point  $D$ ,  $I = 1.93$  mA, above  $I_c$ , the LTSLM response becomes negative.

To explain the bias-dependent sign change, in Fig. 2(c) we show two simulated IVCs of a JJ with the laser beam *off* (blue) and *on* (red) for upward bias sweeps. Heating leads to reduction of both the critical current  $I_c$  and the normal resistance  $R_n$  due to the semiconducting nature of the NbSi barrier, as seen from the experimental IVCs in Fig. 3(a). Simulations are performed within the resistively and capacitively shunted junction model [45,46] with parameters  $I_c = 1.5$  mA,  $R_n = 0.1 \Omega$ , and  $C = 30$

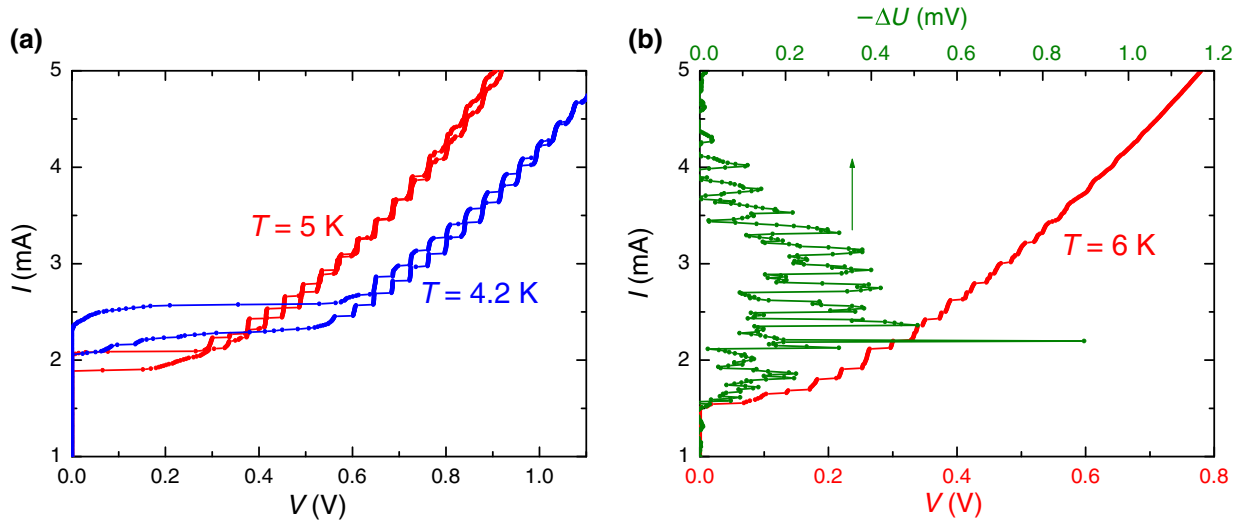


FIG. 3. The transport and radiation measurements of the linear array. (a)  $I$ - $V$  characteristics at different temperatures. (b) The IVC at  $T = 6$  K (red) and the simultaneously measured detector signal (olive curve). The appearance of the resonant step structure in the IVCs is clearly seen. The detected EM power is correlated with the step structure.

pF without laser heating and  $I_c^* = 1.0$  mA,  $R_n^* = 0.07$   $\Omega$ , and  $C = 30$  pF with laser heating. It is seen that at low bias,  $I < I_c^*$ , there is no response,  $\Delta U = 0$ ; at intermediate bias,  $I_c^* < I < I_c$ , the LTSLM response is positive due to suppression of the critical current; and at high bias,  $I > I_c$ , it is negative due to reduction of  $R_n$  by laser heating. With increasing bias, the LTSLM response also increases. For example, the average response at point *A* is  $\Delta U(A) \simeq 30$   $\mu$ V and at point *B* is  $\Delta U(B) \simeq 50$   $\mu$ V.

The LTSLM images in Fig. 2(b) reveal also some nonuniformity of the JJs in the array. For example, although in images A and B most of the JJs exhibit a positive response, some junctions, marked by rectangles in image B, do not respond,  $\Delta U \simeq 0$ . These passive JJs have higher critical currents and remain in the superconducting state even during laser heating. When  $I$  becomes closer to  $I_c$ , more JJs respond to laser irradiation because more JJs switch to the resistive state, as seen from comparison of images A–C. The passive junctions start to show a negative response at bias points *C* and *D*, indicating that their  $I_c \simeq 2$  mA is about 30% higher than for the rest of the JJs. In images A and B, corresponding to  $I < I_c$ , we also observe enhanced sporadic noise due to thermal fluctuations of the switching current [47]. This type of noise disappears at  $I > I_c$  in images C and D.

### III. RESULTS

#### A. Transport and emission characteristics of arrays

Figure 3(a) presents IVCs of the linear array measured in a  $^4$ He dewar at different temperatures. The two lines for each temperature represent up (higher switching current) and down (lower retrapping current) bias sweeps. The

IVCs exhibit hysteresis, presumably of thermal origin. The most-prominent feature of the IVCs is a series of current steps, as reported earlier for similar arrays [17,18,33]. The steps do not occur for a single JJ [34]. Therefore, they are caused by some cavity-mode resonances in the wiring of the array and not in the junctions. Thus, they depend on the electrode and array geometry. At lower temperature,  $T = 4.2$  K, the steps form a regular equidistant structure with spacing  $\Delta V \simeq 39$  mV. The red line in Fig. 3(b) shows the upward part of the IVC at an elevated temperature,  $T = 6$  K. Here the step structure becomes less regular at high bias, presumably due to progressive self-heating.

The estimated step spacing  $\Delta V \simeq 39$  mV corresponds to a characteristic resonant frequency  $f_r = 2e\Delta V/hN_I \simeq 11.4$  GHz. Such a low frequency may originate only from geometrical resonances in the long,  $L_l \simeq 5$  mm, straight lines of the array; see Fig. 1(a). The resonant frequency,  $f_r = c/2L_l\sqrt{\epsilon^*}$ , where  $c$  is the speed of light in a vacuum, yields the effective dielectric permittivity  $\epsilon^* \simeq 6.9$ , which is close to the simple estimation of the static effective permittivity [48]:  $\epsilon_0^* = (\epsilon_s + 1)/2 = 6.5$ , where  $\epsilon_s = 11.9$  is the dielectric permittivity of silicon.

The olive line (top axis) in Fig. 3(b) represents the detector response of the InSb bolometer, measured simultaneously with the corresponding IVC under conditions similar to our LTSLM setup ( $T = 6$  K,  $I_c \simeq 1.5$  mA, sample cooling by  $^4$ He vapor). The detector response is proportional to the absorbed Josephson radiation power. It exhibits profound modulation correlated with the step structure in the IVC. The maximum emission occurs in the range  $I = 2$ – $2.5$  mA. At high bias  $I > 3.5$  mA, the emission peaks start to decay together with step amplitudes due to self-heating.

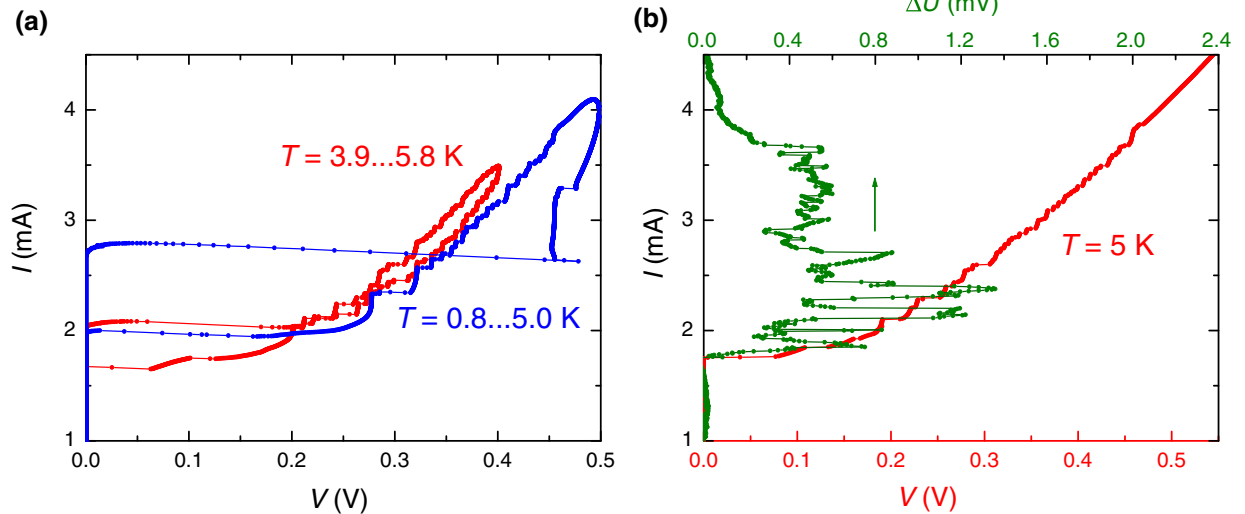


FIG. 4. The transport and radiation measurements of the meandering array. (a)  $I$ - $V$  characteristics at different temperatures measured in a  $^3$ He cryostat with a base temperature 0.8 K (navy) and 3.5 K (red). (b) The IVC at  $T = 5$  K (red) and the simultaneously measured detector signal (olive curve).

Figure 4 presents similar characteristics for the meandering array. They also exhibit distinct resonant steps. However, the step structure is much finer than for the linear array. Since the steps are more pronounced at low  $T$ , the IVCs in Fig. 4(a) are obtained in a  $^3\text{He}$  cryostat. Unfortunately higher resolution comes at the expense of worse thermal stability due to the low cooling power and heat capacitance of the  $^3\text{He}$  stage. A considerable temperature rise during measurements, noted in Fig. 4(a), causes some irregularities and hysteresis. Nevertheless, such measurements allow evaluation of the characteristic step voltage: we observe 32 steps in the range from 0.21 to 0.44 V for both IVCs in Fig. 4(a). This yields  $\Delta V \simeq 7.2$  mV, which is much smaller than for the linear array.

Figure 4(b) presents the results of transport and radiation characterization of a meandering array performed under conditions similar to the LTSLM setup ( $T \simeq 5$  K and sample in  $^4\text{He}$  vapor). The bolometer response  $\Delta U(I)$  is oscillating at  $I < 2.7$  mA with maxima corresponding to certain current steps. In the range  $I = 2.7\text{--}3.7$  mA, the  $\Delta U(I)$  oscillations are more frequent but have lower amplitude, as do the steps in the IVC. At  $I > 3.7$  mA, the oscillations and steps disappear and  $\Delta U(I)$  decays monotonously.

### B. LTSLM of the linear array

Figure 5(a) shows the IVC of the linear array recorded during the LTSLM measurements at the base temperature  $T \simeq 6$  K. Figure 5(b) presents LTSLM images  $\Delta U(x, y)$  of a part of the array at four bias currents, marked in

Fig. 5(a). The scale is the same as in Fig. 2(b). At the lowest bias point,  $A$ ,  $I = 2.0$  mA,  $V \simeq 0.33$  V, few junctions with higher  $I_c$  are still in the superconducting state (pink and blue spots). Otherwise there is no well-defined spatial variation of the array response. At a slightly higher bias point,  $B$ ,  $I = 2.17$  mA,  $V \simeq 0.371$  V, a certain alternation with maxima and minima of  $\Delta U(x, y)$  along the  $x$  direction appears in the three middle lines. At point  $C$ ,  $I = 2.37$  mA,  $V \simeq 0.409$  V, a clear standing-wave pattern develops in the whole array. It has an antisymmetric modulation with maxima in one line corresponding to minima in the neighbor lines. This is demonstrated in detail in Fig. 5(c), which presents averaged scans of  $\Delta U(x)$  along each of the three middle lines of the array (blue) together with fitting curves (red). An additional minor increase of the bias current to point  $D$ ,  $I \simeq 2.4$  mA,  $V \simeq 0.412$  V, leads to a visible reconstruction of the standing-wave pattern. Here it becomes almost symmetric with aligned maxima and minima in all the lines.

The increase of voltage leads to the growth of the Josephson frequency and a reduction of the wavelength of EM radiation. Indeed, such a tendency can be traced from Fig. 5(b). The Josephson frequencies at points  $B$ ,  $C$ , and  $D$  are  $f(B) \simeq 107.8$  GHz,  $f(C) \simeq 119.0$  GHz, and  $f(D) \simeq 119.9$  GHz, respectively. The corresponding periods of the standing waves are  $\Delta x(B) = 0.53$  mm,  $\Delta x(C) = 0.47$  mm, and  $\Delta x(D) = 0.46$  mm. Since LTSLM probes only the EM amplitude, the EM wavelength is twice the period of the LTSLM image,  $\lambda = 2\Delta x$ . The observed decrease of  $\lambda$  with increasing  $f$  follows a simple relation  $\lambda = c/f\sqrt{\epsilon^*}$ , with  $\epsilon^* = 7.1 \pm 0.3$ , consistent with the estimation above from the step voltages in the IVC.

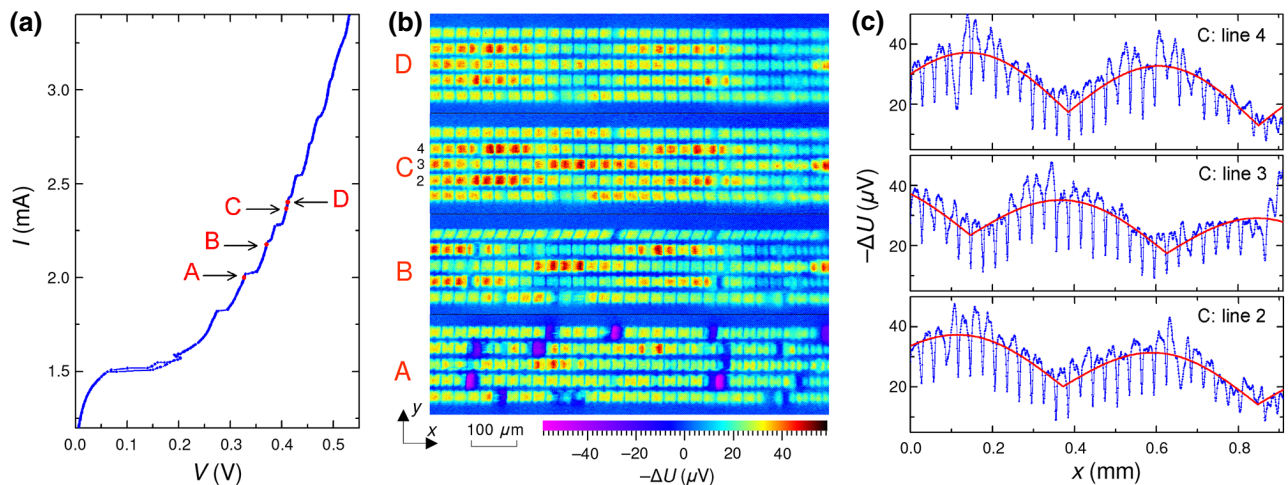


FIG. 5. LTSLM analysis of the linear JJ array at  $T \sim 6$  K. (a)  $I$ - $V$  characteristic of the array measured during LTSLM imaging. (b) LTSLM images obtained at four bias points, indicated in (a). The length of scans along  $x$  axis is  $L_x = 0.91$  mm. The scans are stretched about 2 times along the  $y$  axis for better viewing. Development of standing-wave correlations is clearly seen in images B, C, and D. (c) LTSLM response (blue lines) along horizontal array lines 2–4 [from bottom to top as indicated in (b), image C] for image C,  $I = 2.37$  mA. The data are averaged over the width of a strip. Red lines represent fitting curves obtained by the method of least squares. Antisymmetric modulation in neighboring lines is seen.

The observation of a correlated two-dimensional standing-wave order indicates a global synchronization of the whole array. We perform LTSLM scans over a broad bias range along the IVC. However, standing-wave patterns are observed only in a limited bias range from slightly below point *B* to slightly above point *D*. This is qualitatively consistent with a narrow bias range in which significant EM-wave emission occurs from such an array, as shown in Fig. 3(b).

### C. LTSLM of the meandering array

Figure 6(a) shows the IVC of the meandering array recorded during LTSLM measurements at  $T \simeq 5$  K. Figure 6(b) presents LTSLM images at the bias points marked in Fig. 6(a): *A*,  $I = 1.86$  mA,  $V \simeq 144$  mV; *B*,  $I = 1.9$  mA,  $V \simeq 174$  mV; *C*,  $I = 1.95$  mA,  $V \simeq 200$  mV; *D*,  $I = 2.18$  mA,  $V \simeq 263$  mV. The IVC of the meandering array exhibits a hysteresis, presumably due to self-heating. Points *A*–*C* are measured at the reverse part of the IVC within the hysteretic area. LTSLM images are taken at the right end of the array with the same field of view as in Fig. 5(b), which encompasses 22 transverse strips.

Standing-wave patterns in the horizontal direction can be seen in all images in Fig. 6(b). The periodicity  $\Delta x$  gradually decreases with increasing voltage from image *A* to image *D*: in image *A* it is about five transverse strips and in image *D* it is about three. This is in qualitative agreement with the expected decrease of the wavelength with

increasing frequency. However, if we calculate the speed of EM-wave propagation along the  $x$  axis,  $c_x = 2\Delta x f$ , with  $f = 2eV/hN_m$ , we obtain unreasonably low values. For example, at bias point *A* the periodicity along the horizontal axis is  $\Delta x \simeq 200$   $\mu\text{m}$ , which yields  $c_x \simeq 1.8 \times 10^7$  m/s  $\simeq 0.06c$ . This would require a huge dielectric constant  $\varepsilon^* \sim 300$ , which does not make sense. Therefore, the observed standing waves in the meandering array can not be caused by propagation of a volume EM wave in some media. This conclusion is also confirmed by the observation that with changing frequency the nodal areas (blue color) shift within the transverse strips and may start or end at an arbitrary place along the strips; for example, in image *A* they usually start or end at the edges, but in image *C* they start or end in the middle of the strips. Thus, the standing-wave pattern is not periodic along the horizontal  $x$  axis, as would be expected for a straightforward EM-wave propagation in the substrate. Those inconsistencies, revealed by a specific meandering geometry of the array (see Appendix A), provide a clue to understanding the nature of EM waves in our arrays.

In Fig. 6(c) we plot the LTSLM response for image *D* (top) and image *C* (bottom panel) along the meandering line as a function of the overall length of the Nb electrode from the bottom-left corner to the bottom-right corner of the images in Fig. 6(b). From this plot it becomes clear that there is a long-range standing-wave order along the electrode. The periodicity is  $\Delta l = 1.23$  mm for image *C* and  $\Delta l = 0.85$  mm for image *D*. The corresponding phase velocities,  $c^* = 2\Delta l f$ , are approximately  $1.59 \times 10^8$  m/s

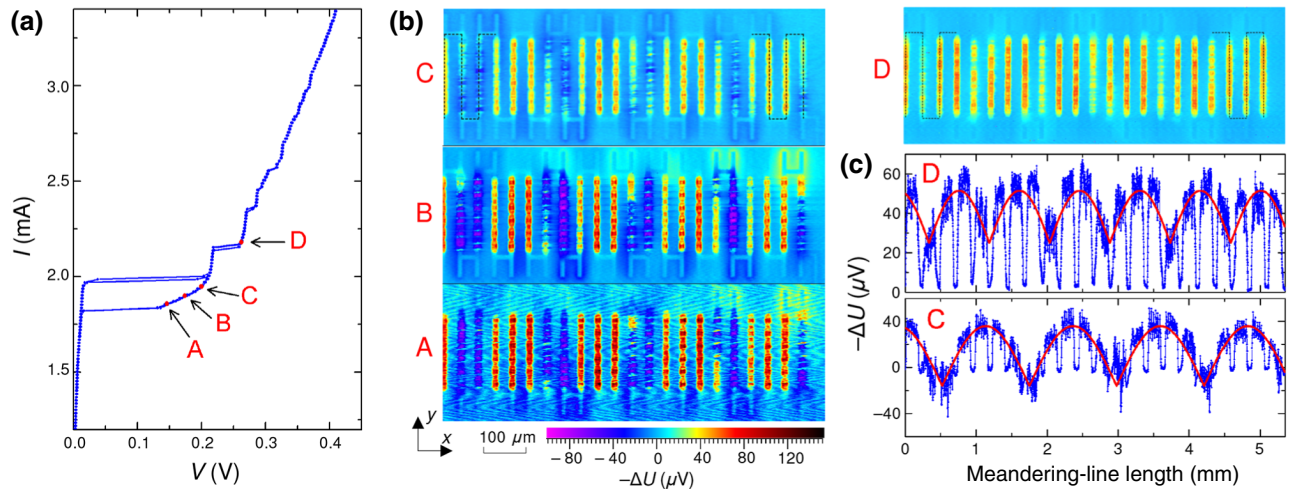


FIG. 6. LTSLM analysis of the meandering array at  $T \sim 5$  K. (a)  $I$ - $V$  characteristic of the array, measured during LTSLM imaging. (b) LTSLM images at different bias points, indicated in (a). The length of scans along the  $x$  axis is  $L_x = 0.91$  mm. The development of a standing-wave pattern is clearly seen. The standing wave is not periodic in the horizontal direction. Dotted lines indicate the start and the end of the track along the length of the meandering line where periodicity of the response is observed. (c) LTSLM responses (blue lines) along the tracks indicated in (b) from the bottom-left corner to the bottom-right corner of the pattern at the bias point *D* (top) and bias point *C* (bottom). The data are averaged over the width of a strip. The red line represents fitting curves obtained by the method of least squares. Clear periodicity along the whole meandering length indicates that standing waves are formed by plasmon-type surface waves propagating along Nb electrodes.

for image C, and  $1.44 \times 10^8$  m/s for image D, which yield a reasonable  $\varepsilon^* \simeq 4.0 \pm 0.3$  (see the additional discussion in Appendix A). This unambiguously proves that EM waves, building the standing wave, are propagating along the electrode line. This is a signature of SEMWs at metal-insulator interfaces [21–31].

Fuhrer confirmation of the SEMW character of standing-wave resonances in the meandering array comes from transport measurements. At low temperatures we observe a very fine step structure in the IVC, see Fig. 4(b), with typical voltage separation  $\Delta V \simeq 7$  mV. This yields a very low primary resonant frequency  $f_r \simeq 2.3$  GHz corresponding to a long resonator length of approximately 3 cm, which is consistent with the total length of the meandering line. This confirms that such resonances are formed by traveling surface waves bound to Nb electrodes.

#### IV. DISCUSSION

There are many known modes of traveling SEMWs [21]. While we cannot provide a decisive distinction of the SEMW modes in our case, we argue that the intermediate value of  $\varepsilon^*$  of approximately 4.0–6.9 between the value for Si (11.9) and the value for a vacuum (1) suggests that they are leaky surface-plasmon-type SEMWs propagating along one interface and leaking energy at the opposite interfaces of the metallic film [23] (see Appendix B). However, the actual subterahertz frequency of the SEMWs involved is well below the plasma frequency. Consequently, they correspond to the linear part of the dispersion relation for surface plasmons. Importantly, the leaky nature of the SEMWs involved both facilitates long-range synchronization of a large array and enables EM-wave emission into open space. All this is a prerequisite for creation of a high-power coherent terahertz oscillator.

##### A. The role of standing waves for super-radiant emission from JJ arrays

As mentioned above, we observe standing waves only in a narrow bias range. Figures 5(b) and 6(b) show the full range of bias in which we see standing waves for the two arrays. At other biases there are no clear standing waves in the LTSLM images, as can be seen from Fig. 2(b). This happens because standing waves appear only when they are actively pumped by the synchronized array and do not appear when oscillations of junctions are not synchronized. Therefore, the observation of standing waves provides unambiguous proof for synchronization of the array.

Bolometric data give complementary information about the role of standing waves for emission from the arrays. Unfortunately, we cannot perform *in situ* measurements of emission inside the LTSLM setup. Instead we try to reproduce LTSLM conditions (temperature and cooling by  $^4\text{He}$  gas) during detection experiments. From Figs. 3(b),

4(b), 5(a), and 6(a) it can be seen that the IVCs from bolometric and LTSLM experiments are fairly similar and have approximately the same  $I_c \simeq 1.5$  mA. Bolometric measurements, olive curves in Figs. 3(b) and 4(b), also indicate that significant emission occurs in only a limited bias range. For the linear array, Fig. 3(b), maximum emission is detected at  $I = 2$ –2.5 mA, which is well correlated with the range of observation of standing-wave patterns by LTSLM, Fig. 5. For the meandering array the two first emission peaks in Fig. 4(b) correlate with the two types of standing waves observed by LTSLM in the same bias ranges at  $I = 1.8$ –1.9 mA, images A–C in Fig. 6(b), and  $I = 2.1$ –2.2 mA, image D in Fig. 6(b). Thus, there is agreement between transport, bolometric, and LTSLM measurements.

From comparison of the bolometric and transport measurements, Figs. 3 and 4, it can be seen that the emission power has peaks at the steps in the IVC, which in turn correspond to the appearance of standing waves in the arrays. Therefore, the peaks correspond to phase-locked states of the arrays and indicate the appearance of coherent super-radiant emission. This conclusion is in full agreement with the anticipated crucial role of standing-wave (cavity-mode) resonances for achieving coherent emission from JJ arrays. As discussed in Refs. [19,20], high-quality-factor,  $Q \gg 1$ , collective cavity-mode resonances have three major contributions to super-radiant emission in JJ arrays: (i) they cause mutual synchronization of junctions by imposing the corresponding order on the array, (ii) they amplify the emission power in proportion to  $Q^2$ , and (iii) they reduce the linewidth of emission in proportion to  $1/Q$ .

##### B. Comparison with flux-flow oscillators

Josephson flux-flow oscillators (FFOs) have excellent characteristics [10,49]. Here we provide a brief comparison of FFOs with the large array-based oscillators considered in this work: can they do more, can they do it better, or can they do it differently?

First of all, the emission power from FFOs is quite low, less than  $1 \mu\text{W}$  (on chip, not far field) [10]. Lower far-field emission from a FFO was also reported recently [49], but this is probably not the main operation mode of the FFO: usually it is used as an on-chip local oscillator (reference signal), which does not need high power. The main motivation for research on JJ arrays is to enhance the power emitted in open space by means of coherent super-radiant emission. As mentioned below, large JJ arrays may indeed provide high-enough off-chip power (approximately 1 mW).

One of the major problems of Josephson oscillators is the large impedance mismatching between the junction and open space [19] because junction sizes are much smaller than the wavelength. In FFOs this problem is solved by

imbedding the oscillator in a microwave transmission line, which delivers the signal to other on-chip elements with small losses [10]. For off-chip emission, proper matching antennas should be implemented [49]. An advantage of very large arrays with sizes much larger than the wavelength is that long electrodes can act as traveling-wave antennas [18,50], thus providing a built-in mechanism of coupling with the far field. Like the Beverage antenna, it is nonresonant and, therefore, broadband.

Tunability is the key advantage of Josephson oscillators [11], including FFOs [10,49]. As shown by bolometric measurements, our arrays can operate in a very broad frequency range. For example, in Ref. [17] the reported range is two octaves, 75–300 GHz. Most often (but not always [18], see Appendix C) the emission has maxima at resonant steps in the IVCs. Therefore, the frequency can be tuned stepwise. This is also the case for FFOs, for which the maximum emission occurs at Fiske steps [10]. In both cases the discreteness of frequency is determined by the size (inversely proportional). The frequency step for our very large arrays with a total active length of approximately 3 cm can be very small, approximately 2.3 GHz. Thus, it is possible to get optimal emission from one array at approximately 100 discrete frequencies. Hypothetically the frequency step can be made arbitrarily small since the size of the array can be increased further. Furthermore, the tunability can become continuous in the case of a pure traveling-wave-antenna-type of operation. Note, however, that standing-wave resonances (and therefore discreteness of frequency) are important for improving (sharpening) the emitted spectra and for increasing the emitted power, as discussed above.

An important advantage of array-based emitters compared with FFOs is that they do not need a magnetic field. The tunability is achieved at zero field.

An outstanding narrow linewidth has been achieved for FFOs [10,49]. Arrays have still to catch up in this respect. Recently we obtained preliminary emission spectra for our arrays, which indicate good monochromaticity of emission.

Finally, we emphasize that this comparison does not imply that array-based oscillators are always better than FFOs. They are not competitive because they have different niche applications (on chip and off chip). Arrays can, of course, also be used as on-chip oscillators [14], if higher power is required. However, we believe that arrays with a large number of JJs are the most-feasible candidates for the creation of tunable Josephson oscillators with high-enough off-chip power.

### C. Performance of and perspectives for large JJ arrays

As mentioned in Sec. I, the main goal of research on large JJ arrays is the creation of tunable, monochromatic, high-power, and compact sources of EM radiation in the terahertz frequency range. In earlier work by Han *et al.*

[14], collective emission from arrays with 500 JJs was reported with the estimated on-chip emission power of  $47 \mu\text{W}$ . The purpose of studying very large arrays with a large number of junctions  $N$  is to increase the coherence factor (proportional to  $N^2$ ) determining the radiation efficiency (ratio of the emitted power to the consumed power) of coherent super-radiant emission [19]. The maximum possible efficiency in the case of perfect impedance matching is 50% [19]. For the arrays studied here with  $N = 1660$  the coherence factor should be an order of magnitude larger than for the arrays studied in Ref. [14]. Recently super-radiant emission from a similar Nb/NbSi/Nb array with  $N = 9000$  JJs was reported, with detected off-chip power  $P \simeq 90 \mu\text{W}$ , by the same InSb bolometer [18]. Taking into account a restricted solid angle of collection of radiation and a limited absorption coefficient, the detection efficiency of our bolometer is not better than 10%–20%. Therefore, a rough estimation indicates that the actual emitted power from the array may well be in the range of 0.5–1 mW, corresponding to a radiation efficiency of approximately 10%. Those are very good numbers.

Thus, the very large arrays that we consider here are indeed promising for the creation of high-power and high-efficiency sources. Yet, the main result of this work is not the observation of high power emission but the discovery of the mechanism of synchronization by surface EM waves. We argue that this opens a possibility for synchronization of very large arrays with sizes much larger than the wavelength, which could greatly increase the emitted power.

## V. CONCLUSIONS

To conclude, synchronization of large oscillator arrays is a challenging problem. In this work we perform simultaneous transport measurements and low-temperature scanning laser microscopy of large arrays with 1500 and 1660 Josephson junctions. Our main result is the observation of standing-wave patterns, indicating global phase-locking of the arrays. From an analysis of the evolution of standing-wave patterns with changing Josephson frequency, we deduce that the patterns are formed by plasmon-type surface EM waves propagating along electrodes at the superconductor-substrate interface. We conclude that such surface waves can facilitate both emission of power and phase-locking of very large oscillator arrays, which is required for the creation of high-power terahertz sources.

## ACKNOWLEDGMENTS

We are grateful to F. Müller and T. Scheller (Physikalisch-Technische Bundesanstalt, Braunschweig, Germany) for sample fabrication. V.M.K. is grateful for hospitality during a sabbatical period at the Moscow Institute of Physics and Technology, arranged via the 5-100 program. This work was supported by the Russian



Science Foundation, Grant No. 20-42-04415 [experimental part: performing the measurements—Figs. 5(a), 5(b), 6(a), and 6(b)], the Russian Foundation for Basic Research, Grant No. 18-02-00912 [theoretical part: fitting—Figs. 5(c) and 6(c)], the State Contract No. 0035-2019-0021 “Transport properties and electrodynamics of nanostructural superconductors and hybrid systems: quantum effects and nonequilibrium states,” the Deutsche Forschungsgemeinschaft via project KL930/17-1, the COST action NANOCOHYBRI (CA16218), the European Union H2020-WIDESPREAD-05-2017-Twinning project SPINTECH under Grant Agreement No. 810144, and the Swedish Research Council, project 2018-04848.

### APPENDIX A: MEANDERING ARRAY AS A SLOW-WAVE SYSTEM

The meandering JJ array investigated in our work is an example of an EM slow-wave system [51], which provides a considerable reduction in the phase velocity of EM waves. The theory of such systems is quite complex, but calculations can be simplified considerably if reflections between elements of the meandering array are negligible. This case seems to be realized for the meandering JJ array because the LTSLM images do not exhibit any signs of reflections of EM waves from the ends of transverse strips. In this case the reduction of phase velocity is determined approximately by the geometrical factor  $1 + w/d \simeq 8$ , where  $w$  is the length of transverse meandering strips and  $d$  is the distance between them. For our meandering array  $w = 290 \mu\text{m}$  and  $d = 40 \mu\text{m}$ , which yields  $c^*/c_x \simeq 8$  for the relation between the velocities along the strips of the array  $c^*$  and along the direction of the meandering array  $c_x$ . From this point of view the meandering line is a decelerated transmission line having a large geometrical deceleration [51].

We also observe that the effective dielectric constant  $\varepsilon^*$  for the meandering array is smaller by a factor of approximately 1.6–1.9 than for the linear array. This may be due to the known effect of reduction of the effective length of bent antennas; see, for example, Ref. [52]. It may lead to the reduction of the actual SEMW propagation length (short-cutting) at the turns of the meandering line and, thus, to overestimation of the wavelength and underestimation of  $\varepsilon^*$ . For the meandering array there is also some variation of the estimated  $\varepsilon^*$  between points A–C, which might be caused by a not-well-known number of active junctions within the hysteresis part of the IVC, which would affect estimation of the Josephson frequency.

### APPENDIX B: DISCUSSION OF SEMW TYPES IN LONG JJ ARRAYS

Traveling waves in an infinite JJ transmission line (traveling-wave antenna) in a homogeneous medium were theoretically investigated in Ref. [50]. Depending on the

relation between the wave number,  $k_t$ , in the transmission line and the wave number,  $k_0$ , in the medium, the traveling wave can be either radiative at a specific angle on both sides of the array ( $k_t < k_0$ ) or completely bound to the array, propagating along it ( $k_t > k_0$ ). The latter is considered as a surface plasmon. In this work the arrays, forming JJ transmission lines, are placed on oxidized silicon substrates. Thus, we should consider wave numbers both in a vacuum,  $k_0$ , and in the substrate,  $k_s$ . The corresponding relations are  $k_t/k_0 = \sqrt{\varepsilon^*} \sim \sqrt{(\varepsilon_s + 1)/2}$  and  $k_s/k_0 = \sqrt{\varepsilon_s}$ ,  $k_0 < k_t < k_s$ . This implies that the traveling SEMW is bound from the vacuum side and is leaky from the substrate side [50]. Such a SEMW is usually referred to as a “leaky surface plasmon” [23].

### APPENDIX C: DISCUSSION OF CORRELATIONS BETWEEN TRANSPORT AND BOLOMETRIC MEASUREMENTS

Despite a general correlation between steps in the IVC and peaks in the bolometric response, a careful analysis of the data in Figs. 3(b) and 4(b) indicates that the detected signal at some steps is quite small, and some steps even correspond to minima of the detector signal. This is, however, not surprising because the detected emission power essentially depends both on the mode of the standing wave and on the position of the detector.

In our experiment the bolometer is placed above the array, normal with respect to the array surface. In the simplest case of an array consisting of a single straight line, mode 1 (half a wavelength along the line) will correspond to a super-radiant maximum of emission in the normal direction due to constructive interference of all junctions. On the other hand, mode 2 (one wavelength along the array) will correspond to zero emission in the normal direction due to also coherent, but destructive interference of junctions. This leads to variation (asymmetry) of emission in a specific direction between odd and even modes [19]. For our arrays, with JJs distributed in a certain two-dimensional order along the substrate, more-complex standing-wave modes with a two-dimensional configuration appear, as seen from Figs. 5(b) and 6(b). The directionality diagram of emission from such two-dimensional modes is quite complex [18,50]. Since the detected emission signal depends both on the mode number (which is quite high, 10–30, in our case) and the position of the detector, the smallness of the emission power at the detector location does not necessarily mean that there is no emission in a wider solid angle.

- 
- [1] M. Tonouchi, Cutting-edge terahertz technology, *Nat. Photonics* **1**, 97 (2007).
  - [2] U. Welp, K. Kadowaki, and R. Kleiner, Superconducting emitters of THz radiation, *Nat. Photonics* **7**, 702 (2013).

- [3] L. Ozyuzer, A. E. Koshelev, C. Kurter, N. Gopalsami, Q. Li, M. Tachiki, K. Kadowaki, T. Yamamoto, H. Minami, H. Yamaguchi, T. Tachiki, K. E. Gray, W.-K. Kwok, and U. Welp, Emission of coherent THz radiation from superconductors, *Science* **318**, 1291 (2007).
- [4] T. M. Benseman, K. E. Gray, A. E. Koshelev, W.-K. Kwok, U. Welp, H. Minami, K. Kadowaki, and T. Yamamoto, Powerful terahertz emission from  $\text{Bi}_2\text{Sr}_2\text{CaCu}_2\text{O}_{8+\delta}$  mesa arrays, *Appl. Phys. Lett.* **103**, 022602 (2013).
- [5] M. Ji, J. Yuan, B. Gross, F. Rudau, D. Y. An, M. Y. Li, X. J. Zhou, Y. Huang, H. C. Sun, Q. Zhu, J. Li, N. Kinev, T. Hatano, V. P. Koshelets, D. Koelle, R. Kleiner, W. W. Xu, B. B. Jin, H. B. Wang, and P. H. Wu,  $\text{Bi}_2\text{Sr}_2\text{CaCu}_2\text{O}_8$  intrinsic Josephson junction stacks with improved cooling: Coherent emission above 1 THz, *Appl. Phys. Lett.* **105**, 122602 (2014).
- [6] T. Kashiwagi, T. Yamamoto, T. Kitamura, K. Asanuma, C. Watanabe, K. Nakade, T. Yasui, Y. Saiwai, Y. Shibano, H. Kubo, K. Sakamoto, T. Katsuragawa, M. Tsujimoto, K. Delfanazari, R. Yoshizaki, H. Minami, R. A. Klemm, and K. Kadowaki, Generation of electromagnetic waves from 0.3 to 1.6 terahertz with a high- $T_c$  superconducting  $\text{Bi}_2\text{Sr}_2\text{CaCu}_2\text{O}_{8+\delta}$  intrinsic Josephson junction emitter, *Appl. Phys. Lett.* **106**, 092601 (2015).
- [7] I. Kakeya and H. Wang, Terahertz-wave emission from  $\text{Bi}2212$  intrinsic Josephson junctions: A review on recent progress, *Supercond. Sci. Technol.* **29**, 073001 (2016).
- [8] R. Kleiner and H. Wang, Terahertz emission from  $\text{Bi}_2\text{Sr}_2\text{CaCu}_2\text{O}_{8+x}$  intrinsic Josephson junction stacks, *J. Appl. Phys.* **126**, 171101 (2019).
- [9] M. Tsujimoto, S. Fujita, G. Kuwano, K. Maeda, A. Elarabi, J. Hawecker, J. Tignon, J. Mangeney, S. S. Dhillon, and I. Kakeya, Mutually synchronized macroscopic Josephson oscillations demonstrated by polarization analysis of superconducting terahertz emitters, ArXiv:2004.07422v1.
- [10] V. P. Koshelets and S. V. Shitov, Integrated superconducting receivers, *Supercond. Sci. Technol.* **13**, R53 (2000).
- [11] E. A. Borodianskyi and V. M. Krasnov, Josephson emission with frequency span 1–11 THz from small  $\text{Bi}_2\text{Sr}_2\text{CaCu}_2\text{O}_{8+\delta}$  mesa structures, *Nat. Commun.* **8**, 1742 (2017).
- [12] S. O. Katterwe, H. Motzkau, A. Rydh, and V. M. Krasnov, Coherent generation of phonon-polaritons in  $\text{Bi}_2\text{Sr}_2\text{CaCu}_2\text{O}_{8+x}$  intrinsic Josephson junctions, *Phys. Rev. B* **83**, 100510(R) (2011).
- [13] V. M. Krasnov, Interlayer tunneling spectroscopy of  $\text{Bi}_2\text{Sr}_2\text{CaCu}_2\text{O}_{8+d}$ : A look from inside on the doping phase diagram of high- $T_c$  superconductors, *Phys. Rev. B* **65**, 140504(R) (2002).
- [14] S. Han, B. Bi, W. Zhang, and J. E. Lukens, Demonstration of Josephson effect submillimeter wave sources with increased power, *Appl. Phys. Lett.* **64**, 1424 (1994).
- [15] P. Barbara, A. B. Cawthorne, S. V. Shitov, and C. J. Lobb, Stimulated Emission and Amplification in Josephson Junction Arrays, *Phys. Rev. Lett.* **82**, 1963 (1999).
- [16] F. Song, F. Müller, R. Behr, and A. M. Klushin, Coherent emission from large arrays of discrete Josephson junctions, *Appl. Phys. Lett.* **95**, 172501 (2009).
- [17] M. A. Galin, A. M. Klushin, V. V. Kurin, S. V. Seliverstov, M. I. Finkel, G. N. Goltsman, F. Müller, T. Scheller, and A. D. Semenov, Towards local oscillators based on arrays of niobium Josephson junctions, *Supercond. Sci. Technol.* **28**, 055002 (2015).
- [18] M. A. Galin, E. A. Borodianskyi, V. V. Kurin, I. A. Shereshevskiy, N. K. Vdovicheva, V. M. Krasnov, and A. M. Klushin, Synchronization of Large Josephson-Junction Arrays by Traveling Electromagnetic Waves, *Phys. Rev. Appl.* **9**, 054032 (2018).
- [19] V. M. Krasnov, Coherent flux-flow emission from stacked Josephson junctions: Nonlocal radiative boundary conditions and the role of geometrical resonances, *Phys. Rev. B* **82**, 134524 (2010).
- [20] V. M. Krasnov, Terahertz electromagnetic radiation from intrinsic Josephson junctions at zero magnetic field via breather-type self-oscillations, *Phys. Rev. B* **83**, 174517 (2011).
- [21] T. K. Sarkar, M. N. Abdallah, M. Salazar-Palma, and W. M. Dyab, Surface plasmons/polaritons, surface waves, and zenneck waves: Clarification of the terms and a description of the concepts and their evolution, *IEEE Antenn. Propag. Mag.* **59**, 78 (2017).
- [22] E. N. Economou, Surface plasmons in thin films, *Phys. Rev.* **182**, 539 (1969).
- [23] J. J. Burke, G. I. Stegeman, and T. Tamir, Surface-polariton-like waves guided by thin, lossy metal films, *Phys. Rev. B* **33**, 5186 (1986).
- [24] E. Ozbay, Plasmonics: Merging photonics and electronics at nanoscale dimensions, *Science* **311**, 189 (2006).
- [25] R. W. Heeres, S. N. Dorenbos, B. Koene, G. S. Solomon, L. P. Kouwenhoven, and V. Zwiller, On-chip single plasmon detection, *Nano Lett.* **10**, 661 (2010).
- [26] M. Kauranen and A. V. Zayats, Nonlinear plasmonics, *Nat. Photonics* **6**, 737 (2012).
- [27] Z. Zalevsky and I. Abdulhalim, *Integrated Nanophotonic Devices* (Elsevier Inc., Oxford, UK, William Andrew, 2014), 2nd ed.
- [28] M. I. Stockman, K. Kneipp, S. I. Bozhevolnyi, S. Saha, A. Dutta, J. Ndukaife, N. Kinsey, H. Reddy, U. Guler, and V. M. Shalaev, *et al.*, Roadmap on plasmonics, *J. Opt.* **20**, 043001 (2018).
- [29] L. Yin, V. K. Vlasko-Vlasov, J. Pearson, J. M. Hiller, J. Hua, U. Welp, D. E. Brown, and C. W. Kimball, Sub-wavelength focusing and guiding of surface plasmons, *Nano Lett.* **5**, 1339 (2005).
- [30] B. Camarota, F. Parage, F. Balestro, P. Delsing, and O. Buisson, Experimental Evidence of One-Dimensional Plasma Modes in Superconducting Thin Wires, *Phys. Rev. Lett.* **86**, 480 (2001).
- [31] K. L. Ngai, Interaction of ac Josephson currents with surface plasmons in thin superconducting films, *Phys. Rev.* **182**, 555 (1969).
- [32] F. Mueller, R. Behr, T. Weimann, L. Palafox, D. Olaya, P. D. Dresselhaus, and S. P. Benz, 1 V and 10 V SNS programmable voltage standards for 70 GHz, *IEEE Trans. Appl. Supercond.* **19**, 981 (2009).
- [33] F. Song, F. Müller, T. Scheller, A. Semenov, M. He, L. Fang, H. W. Hübers, and A. M. Klushin, Compact tunable sub-terahertz oscillators based on Josephson junctions, *Appl. Phys. Lett.* **98**, 142506 (2011).
- [34] D. Olaya, P. D. Dresselhaus, S. P. Benz, A. Herr, Q. P. Herr, A. G. Ioannidis, D. L. Miller, and A. W. Kleinsasser, Digital circuits using self-shunted Nb/

- $\text{Nb}_x\text{Si}_{1-x}/\text{Nb}$  Josephson junctions, *Appl. Phys. Lett.* **96**, 213510 (2010).
- [35] B. Mayer, T. Doderer, R. P. Huebener, and A. V. Ustinov, Imaging of one- and two-dimensional Fiske modes in Josephson tunnel junctions, *Phys. Rev. B* **44**, 12463 (1991).
- [36] C. A. Kruelle, T. Doderer, D. Quenter, R. R. Huebener, R. Pöpel, and J. Niemeyer, Standing wave patterns of microwaves propagating in Josephson tunnel junctions with integrable and chaotic billiard geometries, *Phys. D* **78**, 214 (1994).
- [37] D. Quenter, A. V. Ustinov, S. G. Lachenmann, T. Doderer, R. P. Huebener, F. Müller, J. Niemeyer, R. Pöpel, and T. Weimann, Spatially resolved flux flow in long-overlap Josephson tunnel junctions, *Phys. Rev. B* **51**, 6542 (1995).
- [38] R. Gerber, D. Quenter, T. Doderer, C. A. Kruelle, R. P. Huebener, F. Müller, J. Niemeyer, R. Pöpel, and T. Weimann, Quantitative measurement of the microwave distribution in superconducting tunnel junctions, *Appl. Phys. Lett.* **66**, 1554 (1995).
- [39] H. B. Wang, S. Guenon, J. Yuan, A. Iishi, S. Arisawa, T. Hatano, T. Yamashita, D. Koelle, and R. Kleiner, Hot Spots and Waves in  $\text{Bi}_2\text{Sr}_2\text{CaCu}_2\text{O}_8$  Intrinsic Josephson Junction Stacks: A Study by Low Temperature Scanning Laser Microscopy, *Phys. Rev. Lett.* **102**, 017006 (2009).
- [40] A. Laub, M. Keck, T. Doderer, R. P. Huebener, T. Traeuble, R. Dolata, T. Weimann, and J. Niemeyer, The influence of the critical current spread on the frequency locking of Josephson junctions in two-dimensional arrays, *J. Appl. Phys.* **83**, 5302 (1998).
- [41] M. Keck, T. Doderer, R. P. Huebener, T. Traeuble, R. Dolata, T. Weimann, and J. Niemeyer, Spatially resolved detection of phase locking in Josephson junction arrays, *Appl. Supercond.* **6**, 297 (1998).
- [42] S. G. Lachenmann, T. Doderer, D. Hoffmann, R. P. Huebener, P. A. A. Booi, and S. P. Benz, Observation of vortex dynamics in two-dimensional Josephson-junction arrays, *Phys. Rev. B* **50**, 3158 (1994).
- [43] R. Werner, A. Yu. Aladyshkin, S. Guénon, J. Fritzsche, I. M. Nefedov, V. V. Moshchalkov, R. Kleiner, and D. Koelle, Domain-wall and reverse-domain superconducting states of a Pb thin-film bridge on a ferromagnetic  $\text{BaFe}_{12}\text{O}_{19}$  single crystal, *Phys. Rev. B* **84**, 020505(R) (2011).
- [44] R. Werner, A. Yu. Aladyshkin, I. M. Nefedov, A. V. Putilov, M. Kemmler, D. Bothner, A. Loerincz, K. Ilin, M. Siegel, R. Kleiner, and D. Koelle, Edge superconductivity in Nb thin film microbridges revealed by electric transport measurements and visualized by scanning laser microscopy, *Supercond. Sci. Technol.* **26**, 095011 (2013).
- [45] W. C. Stewart, Current-voltage characteristics of Josephson junctions, *Appl. Phys. Lett.* **12**, 277 (1968).
- [46] D. E. McCumber, Tunneling and weak-link superconductor phenomena having potential device applications, *J. Appl. Phys.* **39**, 2503 (1968).
- [47] V. M. Krasnov, T. Golod, T. Bauch, and P. Delsing, Anticorrelation between temperature and fluctuations of the switching current in moderately damped Josephson junctions, *Phys. Rev. B* **76**, 224517 (2007).
- [48] K. C. Gupta, R. Garg, I. Bahl, and P. Bhartia, in *Microstrip Lines and Slotlines* (Artech House, USA, 1996), 2nd ed., Chap. 1, 5, 7.
- [49] N. V. Kinev, K. I. Rudakov, L. V. Filippenko, A. M. Baryshev, and V. P. Koshelets, Terahertz source radiating to open space based on the superconducting flux-flow oscillator: Development and characterization, *IEEE Trans. Terahertz Sci. Technol.* **9**, 557 (2019).
- [50] V. V. Kurin, N. K. Vdovicheva, and I. A. Shereshevsky, Josephson traveling-wave antennas, *Radiophys. Quantum Electron.* **59**, 922 (2017).
- [51] D. A. Gandolfo, A. Boornard, and L. C. Morris, Superconductive microwave meander lines, *J. Appl. Phys.* **39**, 2657 (1968).
- [52] D. M. Dobkin, in *The RF in RFID: Passive UHF RFID in Practice* (Newnes, USA, 2008), 1st ed., Chap. 7.